Microscopic description of quadrupole-octupole coupling in neutron-rich actinides and superheavy nuclei with the Gogny-D1M energy density functional

R. Rodríguez-Guzmán*
Department of Physics, Kuwait University, 13060 Kuwait, Kuwait

L. M. Robledo†
Center for Computational Simulation, Universidad Politécnica de Madrid, Campus Montegancedo, 28660 Boadilla del Monte, Madrid, Spain
and Departamento de Física Teórica and CIAFF, Universidad Autónoma de Madrid, 28049 Madrid, Spain

(Received 23 January 2021; accepted 22 March 2021; published 1 April 2021)

The interplay between quadrupole and octupole degrees of freedom is discussed in a series of neutron-rich actinides and superheavy nuclei with $92 \leqslant Z \leqslant 110$ and $186 \leqslant N \leqslant 202$. In addition to the static Hartree-Fock-Bogoliubov approach, dynamical beyond-mean-field correlations are taken into account via both parity restoration and symmetry-conserving generator coordinate method calculations based on the Gogny-D1M energy density functional. Physical properties such as correlation energies, negative-parity excitation energies, as well as reduced transition probabilities $B(E1)$ and $B(E3)$ are discussed in detail. It is shown that, for the studied nuclei, the quadrupole-octupole coupling is weak and to a large extent the properties of negative-parity states can be reasonably well described in terms of the octupole degree of freedom alone.

DOI: 10.1103/PhysRevC.103.044301

I. INTRODUCTION

All over the nuclear chart, the majority of the spherical and/or quadrupole-deformed ground states are reflection symmetric. However, in regions with the given proton and/or neutron numbers (around the so-called octupole magic numbers 34, 56, 88 and 134), the spatial reflection symmetry is broken spontaneously and octupole-deformed ground states are favored energetically [1]. Octupole deformation is also well known to affect the outer fission barriers of atomic nuclei and is the collective variable associated to cluster radioactivity (see, for example, Refs. [2–5]). The search for signatures of octupole correlations has remained an active research field over the years [6–16]. Previous experiments have found evidence for octupole-deformed ground states in ^{144,146}Ba [12,13] and ^{222,224}Ra [14,15] and measured the $E1$ strength in ^{228}Th [16]. Furthermore, a correlation between the Schiff moment [17] and octupole deformation has been found [18], suggesting that octupole-deformed nuclei might represent the best candidates for atomic electric dipole moment measurements.

From a theoretical point of view, various models and approaches have already been employed to study the properties of octupole collectivity. Among them, we can mention the studies of octupole shapes carried out using the macroscopic-microscopic (MM) approach [19–23] or the interacting boson model (IBM) [24–27] with parameters determined using fermion-to-boson mapping procedures starting from mean-field potential energy surfaces (MFPESs), obtained with relativistic and nonrelativistic energy density functionals (EDFs).

Microscopic nonrelativistic and relativistic approaches, both at the mean-field level and beyond, have been widely used to study octupole correlations [28–51]. Those microscopic studies include global surveys looking for octupole-deformed mean-field ground states in even-even nuclei [45–51]. In addition, properties of dynamic octupole correlations have been analyzed in large-scale beyond-mean-field calculations carried out for even-even nuclei and using several parametrizations of the Gogny [52] EDF [50,51]. The results of those calculations indicate that not only static octupole deformation but also dynamical beyond-mean-field octupole correlations have a sizeable impact on physical observables.

The interplay between the two lowest multipole moments characterizing the nuclear shape, namely the quadrupole and octupole degrees of freedom, has been studied in Sm and Gd isotopes with neutron number $84 \leqslant N \leqslant 92$ [53] as well as in actinide nuclei around $N \approx 134$ [54]. Calculations have been carried out using the parametrizations D1S [55], D1M [56], and D1M* [57] of the Gogny-EDF. Both quadrupole and octupole constraints were considered simultaneously to build the MFPESs for the considered nuclei. Those MFPESs exhibited a soft behavior along the octupole direction, indicating that dynamical beyond-mean-field effects should be taken into account. Those beyond-mean-field effects were considered via both parity projection of the intrinsic states and symmetry-conserving quadrupole-octupole configuration mixing calculations, in the spirit of the two-dimensional (2D) generator coordinate method (GCM) [58]. In addition to the systematic of the correlation energies, 1^- excitation energies, $B(E1)$ and $B(E3)$ transition probabilities, the results

*raynerrobertorodriguez@gmail.com
†luis.robledo@uam.es

of Refs. [53,54] indicate that 2D-GCM zero-point quantum fluctuations lead to a dynamically enhanced octupolarity in the studied nuclei. The 2D-GCM framework has also been applied to Rn, Ra, and Th nuclei in Ref. [59].

Octupole correlations in neutron-rich heavy and superheavy nuclei have been the subject of intense scrutiny in recent years [22,32,47–49,60–62]. Those nuclei will not be accessible with future radioactive beam facilities (RBF). However, they represent the territories where the fate of the nucleosynthesis of heavy nuclei is determined and therefore a better understanding of their properties is required, for example, to improve the modeling of fission recycling in neutron star mergers [63,64].

Among the calculations mentioned in the previous paragraph, those based on the NL3*, DD-ME2, DD-PC1, and PC-PK1 relativistic EDFs [47,48], have predicted an island of octupole-deformed nuclei in their ground state centered at $Z \approx 96$, $N \approx 196$. An island of octupolarity has also been found with the SLy6 and SV-min zero-range Skyrme-EDFs but this time centered at $Z \approx 100$, $N \approx 190$ [32]. An intermodel comparison between the NL3*, DD-ME2, DD-PC1, and PC-PK1 covariant EDFs and the UNEDF0, UNEDF1, UNEDF2, SLy4, and SV-min Skyrme-EDFs has been presented in Ref. [49] for $Z \leqslant 110$ and $N \leqslant 210$. It has been concluded that a region of the octupole-deformed ground state exists for $184 < N < 206$. Furthermore, calculations within the MM framework predicted an island of octupole deformation centered at $Z \approx 100$, $N \approx 184$ [22]. Recent MM large-scale calculations for $98 \leqslant Z \leqslant 126$ and $134 \leqslant N \leqslant 192$ predicted octupole-deformed ground states for $N \geqslant 182$ [60]. Additionally, an account of the fission properties of superheavy nuclei with $100 \leqslant Z \leqslant 126$ including very neutron-rich isotopes up to around 4 MeV from the two-neutron driplines has predicted octupole instability for $186 \leqslant N \leqslant 194$ using the Gogny-D1M* EDF [61]. All the aforementioned approaches agree on the existence of an island of octupolarity in neutron-rich actinides and low-Z (i.e., $Z \leqslant 110$) superheavy nuclei, in spite of the differences regarding its location and extension in the (Z, N) plane. However, the predictions of different approaches differ for larger Z values [22,32,48,60–62].

Given the relevance of dynamical octupole correlations and/or symmetry restoration in the properties associated to the octupole degree of freedom pointed out in our previous studies, discussed above, we have decided to apply those techniques to the region of the nuclear chart including actinides and low-Z superheavies. In this work, we study the quadrupole-octupole coupling in neutron-rich even-even nuclei with proton and neutron numbers $92 \leqslant Z \leqslant 110$ and $186 \leqslant N \leqslant 202$. As in previous studies covering other regions of the nuclear chart [53,54], we consider three levels of approximation for each nucleus. First, the constrained Hartree-Fock-Bogoliubov (HFB) approach is used to obtain a set of mean-field HFB wave functions, which are labeled by their intrinsic quadrupole and octupole moments. The energy associated with those HFB states is used to build a mean-field potential energy surface (MFPES) which is a function of both the quadrupole and octupole moments. As discussed later on, those MFPESs often are rather soft along the octupole direction. Some of the studied neutron-rich nuclei display a pronounced competition, i.e., shape coexistence, between reflection-symmetric and reflection-asymmetric configurations. Moreover, in some cases the MFPES exhibits a transitional behavior along the quadrupole direction. Therefore, the HFB approximation can only be considered as a starting point and dynamical correlations stemming from the restoration of the broken parity symmetry (second level) and/or fluctuations in the collective quadrupole and octupole coordinates (third level) have to be taken into account.

The results discussed in this paper have been obtained with the finite-range and density-dependent Gogny-D1M EDF. Such a parametrization, specially tailored to better describe nuclear masses, has already provided a reasonable description of octupole properties [44,50,53,54,59]. However, in order to illustrate the robustness of the 2D-GCM predictions with respect to the underlying Gogny-EDF, we will also discuss results obtained with the D1S, D1M*, and D1M** parametrizations for a selected set of nuclei. The parametrization D1S has been thoroughly tested all over the nuclear chart both at the mean-field level and beyond (see, for example, Ref. [65] and references therein). On the other hand, D1M* and D1M** are newly proposed reparametrizations of D1M with the goal of improving the slope of the symmetry energy while preserving as much as possible other properties of D1M. Details of their fitting protocol can be found in Refs. [57,66].

The paper is organized as follows. The three levels of approximation employed in this study are briefly outlined in Secs. II A and II B. In order to facilitate the discussion, the results obtained with the corresponding approach will be discussed in each section. The HFB results will be discussed in Sec. II A while beyond-mean-field correlations are considered in Sec. II B. First, parity-projected potential energy surfaces (PPPESs) are computed via parity projection of the intrinsic HFB states in Sec. II B 1. This level of approximation is useful to disentangle the relative contribution of parity projection to the total correlation. Second, both parity projection and fluctuations in the collective coordinates are considered via 2D-GCM calculations in Sec. II B 2. Special attention is paid in Sec. II B 2 to the systematic of 1^- energy splittings, correlation energies, and $B(E1)$ and $B(E3)$ transition probabilities in the considered nuclei. Furthermore, in this section, we will discuss the robustness of the 2D-GCM predictions with respect to the considered Gogny-EDF. Finally, Sec. III is devoted to the concluding remarks.

II. RESULTS

The aim of this work is to study the quadrupole-octupole coupling in the neutron-rich nuclei $^{278–294}$U, $^{280–296}$Pu, $^{282–298}$Cm, $^{284–300}$Cf, $^{286–302}$Fm, $^{288–304}$No, $^{290–306}$Rf, $^{292–308}$Sg, $^{294–310}$Hs, and $^{296–312}$Ds. Three levels of approximation have been employed: the HFB [58] scheme with constraints on the (axially symmetric) quadrupole and octupole operators, parity projection of the intrinsic state, and the symmetry-conserving 2D-GCM. In what follows, we briefly outline those approaches, which were used in the past in different regions of the nuclear chart [53,54,59]. The

different results obtained at each level of approximation will be presented and discussed.

A. Mean field

For each of the studied nuclei, we first build the MFPES, i.e., the mean-field energy $E_{\rm HFB}(\mathbf{Q})$ as a function of the $K=0$ multipole deformation moments $\mathbf{Q}=(Q_{20},Q_{30})$. To this end, the HFB equation with constraints on the axially symmetric quadrupole

$$\hat{Q}_{20}=z^2-\tfrac{1}{2}(x^2+y^2) \tag{1}$$

and octupole operator

$$\hat{Q}_{30}=z^3-\tfrac{3}{2}(x^2+y^2)z \tag{2}$$

is solved using an approximate second-order gradient method [67] that guarantees a fast and reliable convergence of the self-consistent HFB procedure. The quadrupole Q_{20} and octupole Q_{30} deformation parameters are defined via the mean values of the operators $\hat{Q}_{20}$ and $\hat{Q}_{30}$ in the corresponding HFB states. From the deformations Q_{20} and Q_{30}, one can easily compute [39] the deformations parameters β_2 and β_3 as

$$\beta_l=\frac{\sqrt{4\pi(2l+1)}}{3R_0^lA}Q_{l0} \tag{3}$$

where $R_0=1.2A^{1/3}$ and A is the mass number. For example, for $A=294$ a quadruple deformation $Q_{20}=10$ b is equivalent to $\beta_2=0.141$ and an octupole deformation $Q_{30}=1$ b$^{3/2}$ is equivalent to $\beta_3=0.021$.

In order to alleviate the already substantial computational effort, both axial and time-reversal symmetries have been kept as self-consistent symmetries. Aside from the usual mean-field constrains on the proton and neutron numbers, the center of mass is fixed at the origin to avoid spurious effects associated with its motion [44,53,54,59]. To grant convergence for the studied physical quantities, the HFB quasiparticle operators $(\hat{\alpha}_k^\dagger,\hat{\alpha}_k)$ [58] have been expanded in a (deformed) axially symmetric harmonic oscillator (HO) basis $(\hat{c}_l^\dagger,\hat{c}_l)$ containing 17 major shells.

The MFPESs obtained for the isotopes $^{288-304}$No are shown in Fig. 1 as illustrative examples. In our calculations, the Q_{20} grid -20 b $\leqslant Q_{20}\leqslant 50$ b (with a step $\delta Q_{20}=1$ b) and the Q_{30} grid 0 b$^{3/2}\leqslant Q_{30}\leqslant 20$ b$^{3/2}$ (with a step $\delta Q_{30}=0.5$ b$^{3/2}$) have been employed. Along the Q_{20} direction, there is a shape and phase transition from a spherical ground state in ^{288}No to well quadrupole-deformed ground states in heavier isotopes. For $^{290-294}$No, the MFPESs exhibit a transitional behavior along the Q_{20} direction. Similar results are obtained for other isotopic chains. As can be seen from Figs. 2(a1)–2(a5) and 2(d1)–2(d5), the ground-state quadrupole deformations $Q_{20,GS}$ are within the range 0 b $\leqslant Q_{20,GS}\leqslant 30$ b.

The MFPESs show octupole-deformed minima in some No isotopes with the minima occurring always at small quadrupole deformations. A typical example is ^{290}No, which is octupole deformed and almost spherical. When the isotopes of No acquire a larger quadrupole deformation, the octupole-deformed minimum vanishes and the ground state becomes reflection symmetric with a rather soft MFPES along the Q_{30} direction. This pattern repeats in all the other isotopes considered in this work as can be deduced from Fig. 2. We observe there that octupole-deformed HFB ground states are found in $^{284-290}$U, $^{284-290}$Pu, $^{286-292}$Cm, $^{286-292}$Cf, $^{288-294}$Fm, $^{288-294}$No, ^{292,294}Rf, ^{294,296}Sg, ^{296}Hs, and ^{298}Ds with 1 b$^{3/2}\leqslant Q_{30,GS}\leqslant$ 7 b$^{3/2}$ [see Figs. 2(b1)–2(b5) and 2(e1)–2(e5)]. These results indicate that, as in previous studies [22,32,47–49,60], an island of octupole-deformed neutron-rich actinides and low-Z superheavy nuclei is found in our HFB calculations based on the the Gogny-D1M EDF. Similar results, not shown here, have also been obtained with the D1S, D1M*, and D1M** parametrizations.

The HFB energy gained by breaking reflection symmetry in the ground state, defined as

$$\Delta E_{\rm CORR,HFB}=E_{{\rm HFB},Q_{30}=0}-E_{{\rm HFB},GS}, \tag{4}$$

is plotted in Figs. 2(c1)–2(c5) and 2(f1)–2(f5). The largest values of $\Delta E_{\rm CORR,HFB}$ correspond to $N=194$ (U), $N=192$ (Pu, Cm, Cf, and Fm), $N=190$ (No and Rf), and $N=188$ (Sg, Hs, and Ds). The maximum value of 1.8 MeV corresponds to ^{290}Cf. The relatively small $\Delta E_{\rm CORR,HFB}$ energies reflect the softness along the Q_{30} direction in the MFPESs of nuclei with an octupole-deformed HFB ground state.

For some No isotopes, the MFPESs (see Fig. 1) exhibit a pronounced competition, i.e., shape coexistence, between reflection-symmetric and reflection-asymmetric minima. For example, in the case of ^{296}No the energy difference between the global reflection-symmetric $(Q_{20,GS},Q_{30,GS})=(22\text{ b},0)$ and local reflection-asymmetric $(Q_{20},Q_{30})=(10\text{ b},7\text{ b}^{3/2})$ minima amounts to just 210 keV. Such a shape coexistence is also observed in other isotopic chains.

Before concluding this section, we turn our attention to single-particle properties. As it is well known, atomic nuclei "avoid" regions with high single-particle level densities (Jahn-Teller effect) and therefore the plots of single-particle energies (SPEs) as a function of quadrupole or octupole moment help us to identify regions where energy gaps (i.e., low-level density regions) favor the appearance of deformed minima. For this purpose, we have chosen to plot the eigenvalues of the Routhian $h=t+\Gamma-\lambda_{Q_{20}}Q_{20}-\lambda_{Q_{30}}Q_{30}$, where t is the kinetic energy and Γ is the Hartree-Fock field. The term $\lambda_{Q_{20}}Q_{20}+\lambda_{Q_{30}}Q_{30}$ contains the Lagrange multipliers used to enforce the corresponding quadrupole and octupole constraints. The single-particle energies obtained in the ^{292}No case are plotted in Figs. 3 and 4, for protons and neutrons separately, as functions of the quadrupole moment. The plot of Fig. 3 corresponds to zero octupole deformation, and therefore the parity of each single-particle orbital is identified with the use of full (positive-parity) and dashed (negative-parity) lines. On the other hand, Fig. 4 corresponds to the same kind of plot but in this case we have taken an octupole deformation $Q_{30}=6$ b$^{3/2}$ that roughly corresponds with the position of the octupole deformed minima. In the latter, parity is not a good quantum number. Finally, the corresponding Fermi levels are plotted with a thick dotted red line. The first thing we notice in Fig. 3 is the presence of $\Delta j=\Delta l=3$ orbitals around the Fermi level both for protons $(i_{13/2}-f_{7/2})$ and neutrons $(k_{17/2}-h_{11/2})$. The presence of these opposite-parity $\Delta J=\Delta l=3$ pairs of orbitals is a natural requirement for

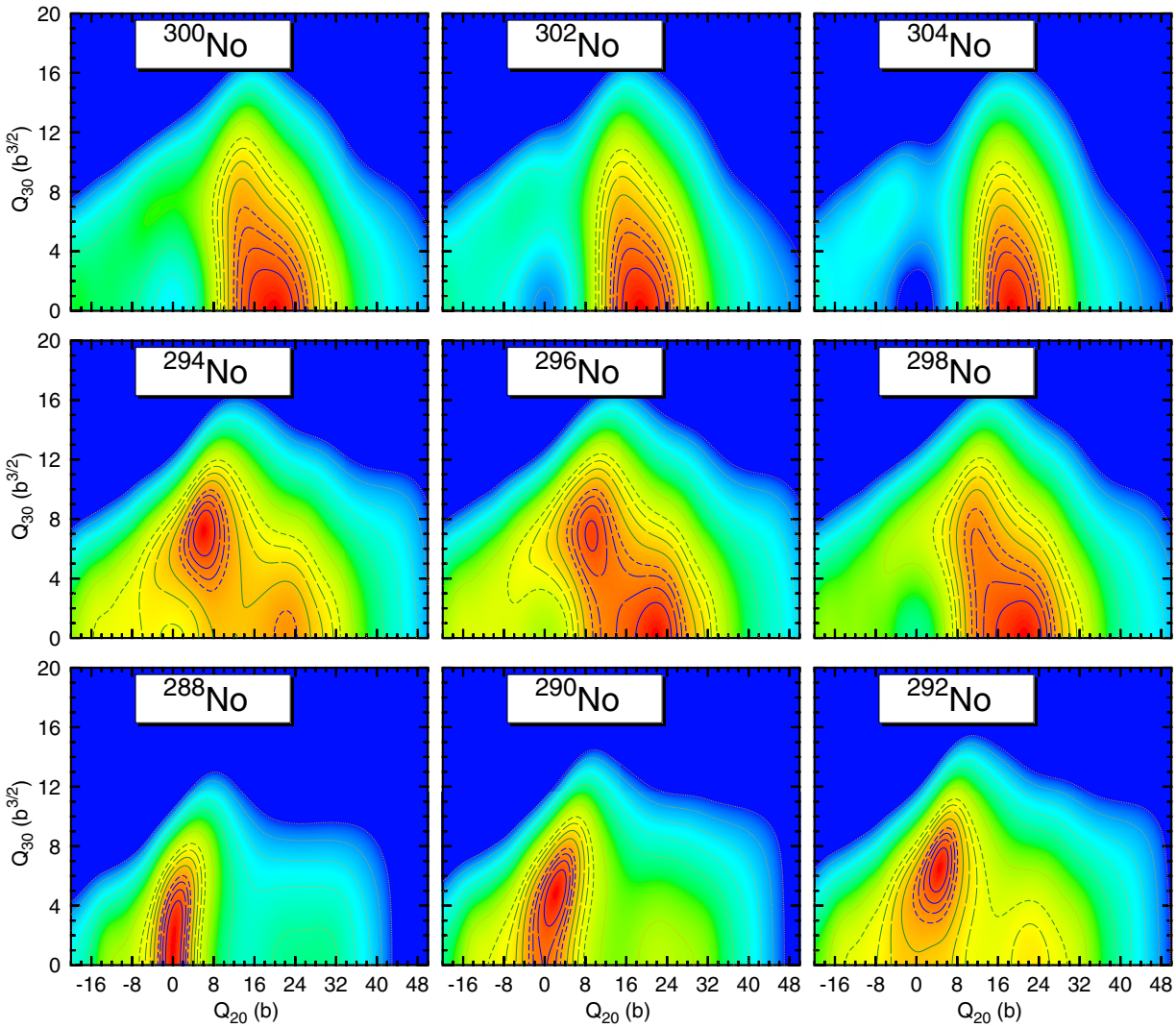

FIG. 1. MFPESs computed with the Gogny-D1M EDF for the isotopes $^{288–304}$No. Dark blue contour lines extend from 0.25 up to 1 MeV above the ground-state energy in steps of 0.25 MeV in the ascending sequence of full, long-dashed, medium-dashed, and short-dashed. Dark green contour lines extend 1.5 up to 3 MeV above the ground state in steps of 0.5 MeV with the same sequence of full, long-dashed, medium-dashed, and short-dashed as before. From there on, orange dotted contour lines are drawn in steps of 1 MeV. The color code spans a range of 10 MeV with red corresponding to the lowest energy and blue corresponding to an energy 10 MeV above. The intrinsic HFB energies are symmetric under the exchange $Q_{30} \to -Q_{30}$. For $A = 294$, a quadruple deformation $Q_{20} = 10$b is equivalent to $\beta_2 = 0.141$ and an octupole deformation $Q_{30} = 1\text{b}^{3/2}$ is equivalent to $\beta_3 = 0.021$. For more details, see the main text.

the existence of octupole-deformed minima. For protons and neutrons, there are gaps in the spectra at the spherical configuration relatively close to the Fermi level: Those gaps are the precursors of the near spherical octupole-deformed minima observed for neutron numbers $N = 186$–192. The deformed minima observed for larger N values at $Q_{20} \approx 18$ b are due to gaps opening up at that deformation. In Fig. 4, we depict the same type of plot but for $Q_{30} = 6\ \text{b}^{3/2}$. At $Q_{20} = 0$, we have included the labels of the spherical orbitals at the same place where they are located in the $Q_{30} = 0$ plot to show the strong impact of parity mixing. We observe how large shell gaps open up at $Q_{20} = 0$ as a consequence of parity mixing that are responsible for the near spherical octupole-deformed minima obtained for $N = 186$–192. On the other hand, for $Q_{20} \approx 18$ b there are no clear gaps in the spectrum, in agreement with the fact that there are no octupole-deformed minima for that value of the quadrupole moment.

B. Beyond-mean-field correlations

As discussed in the previous section, the softness of the MFPESs along the octupole direction as well as the existence in some cases of coexisting minima point toward the key role of dynamical beyond-mean-field correlations, i.e., symmetry restoration and/or quadrupole-octupole configuration mixing in the properties of the ground state and collective negative-parity states in the studied nuclei. Since the octupole is the softest mode, the spatial reflection symmetry is the most important invariance to be restored. It would be desirable to

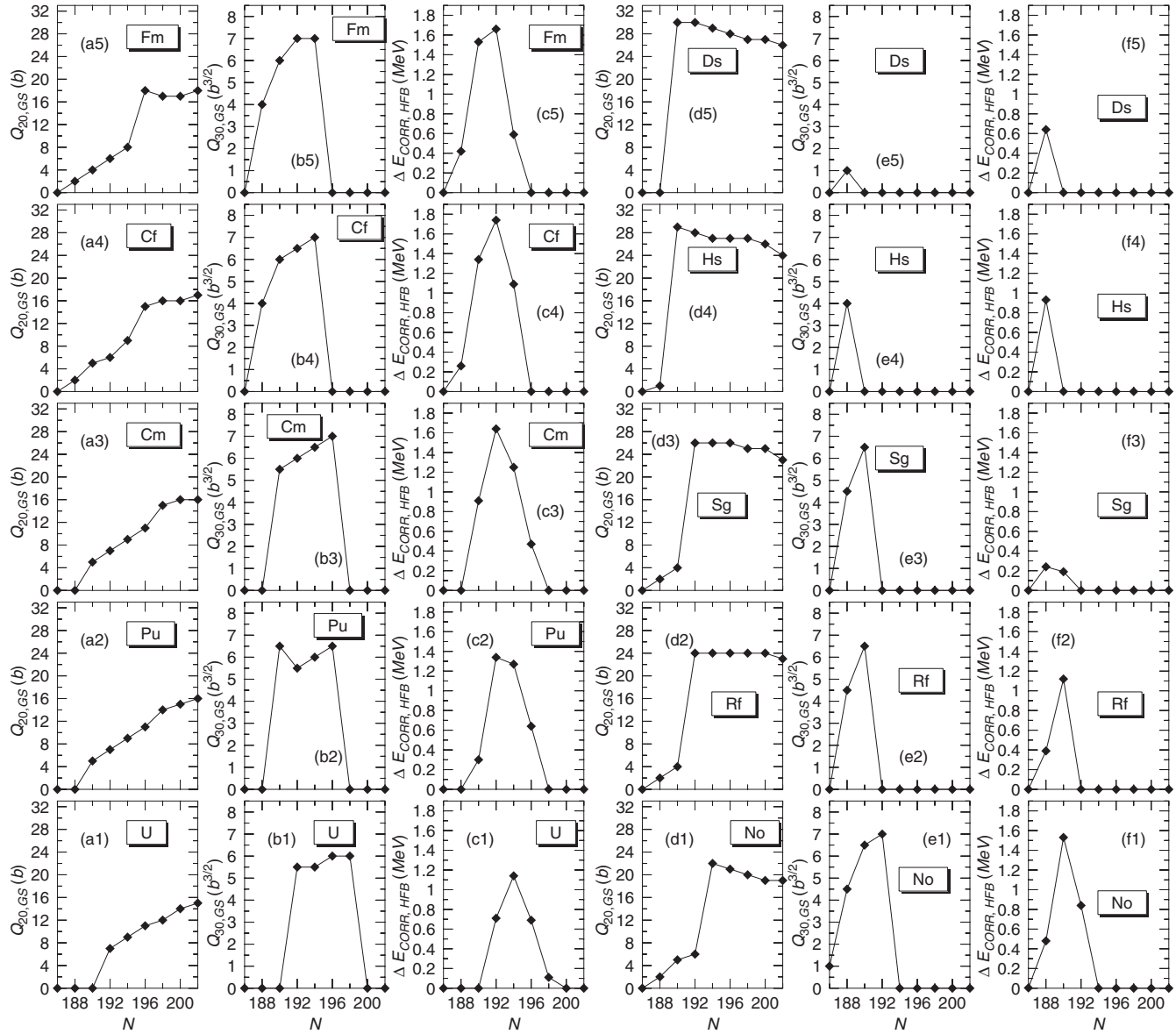

FIG. 2. The mean-field ground-state quadrupole [panels (a1)–(a5) and (d1)–(d5)] and octupole [panels (b1)–(b5) and (e1)–(e5)] deformations as well as the octupole correlation energies $\Delta E_{\mathrm{CORR,HFB}}$ [panels (c1)–(c5) and (f1)–(f5)] from Eq. (4) are plotted, as functions of the neutron number, for the nuclei $^{278–294}$U, $^{280–296}$Pu, $^{282–298}$Cm, $^{284–300}$Cf, $^{286–302}$Fm, $^{288–304}$No, $^{290–306}$Rf, $^{292–308}$Sg, $^{294–310}$Hs, and $^{296–312}$Ds. Results have been obtained with the Gogny-D1M EDF.

restore also both the rotational and particle number symmetries. However, such a gigantic task is out of the scope of an exhaustive survey like the one discussed in this paper for several technical reasons (for example, the large number of HO shells used and the number of degrees of freedom required in the GCM ansatz).

1. Parity symmetry restoration

In order to restore the spatial reflection symmetry broken by the HFB states $|\Phi(\mathbf{Q})\rangle$ with nonzero octupole deformation, we resort to parity projection; i.e., we build the parity-conserving states $|\Phi^{\pi}(\mathbf{Q})\rangle = \hat{\mathcal{P}}^{\pi}|\Phi(\mathbf{Q})\rangle$ by applying on the intrinsic state the parity projector

$$\hat{\mathcal{P}}^{\pi} = \tfrac{1}{2}(1 + \pi\hat{\Pi}), \tag{5}$$

where $\pi = \pm 1$ is the desired parity quantum number. The energies $E_{\pi}(\mathbf{Q})$, associated with the states $|\Phi^{\pi}(\mathbf{Q})\rangle$, define the PPPESs. They read

$$E_{\pi}(\mathbf{Q}) = \frac{\langle\Phi(\mathbf{Q})|\hat{H}[\rho(\vec{r})]|\Phi(\mathbf{Q})\rangle}{2\langle\Phi(\mathbf{Q})|\hat{\mathcal{P}}^{\pi}|\Phi(\mathbf{Q})\rangle} + \pi\frac{\langle\Phi(\mathbf{Q})|\hat{H}[\theta(\vec{r})]\hat{\Pi}|\Phi(\mathbf{Q})\rangle}{2\langle\Phi(\mathbf{Q})|\hat{\mathcal{P}}^{\pi}|\Phi(\mathbf{Q})\rangle}$$

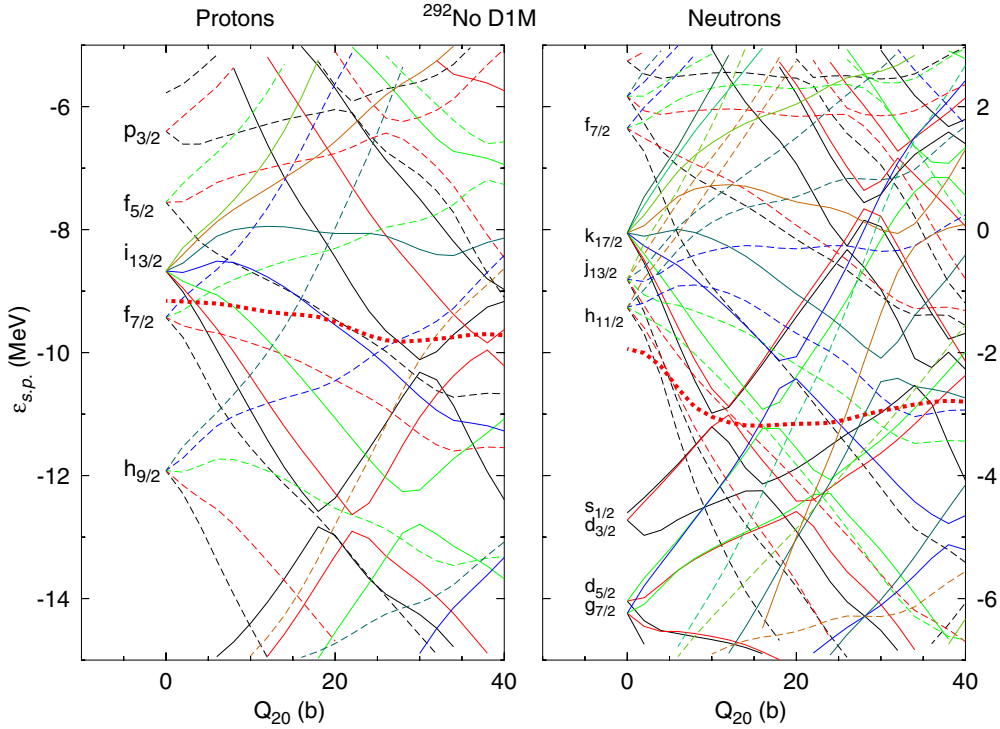

FIG. 3. Single-particle energies for protons (left panel) and neutrons (right panel) as a function of the quadrupole moment and for reflection symmetric $Q_{30} = 0$ shapes. The spherical quantum numbers at Q_{20} are also indicated in the plot. The color code is associated with the K value of the orbital (black, $K = 1/2$; red, $K = 3/2$; green, $K = 5/2$; blue, $K = 7/2$; forest green, $K = 9/2$; brown, $K = 11/2$, etc.). Positive-parity (negative-parity) orbitals are plotted as full (dashed) curves. The Fermi level is represented with a thick dotted red line.

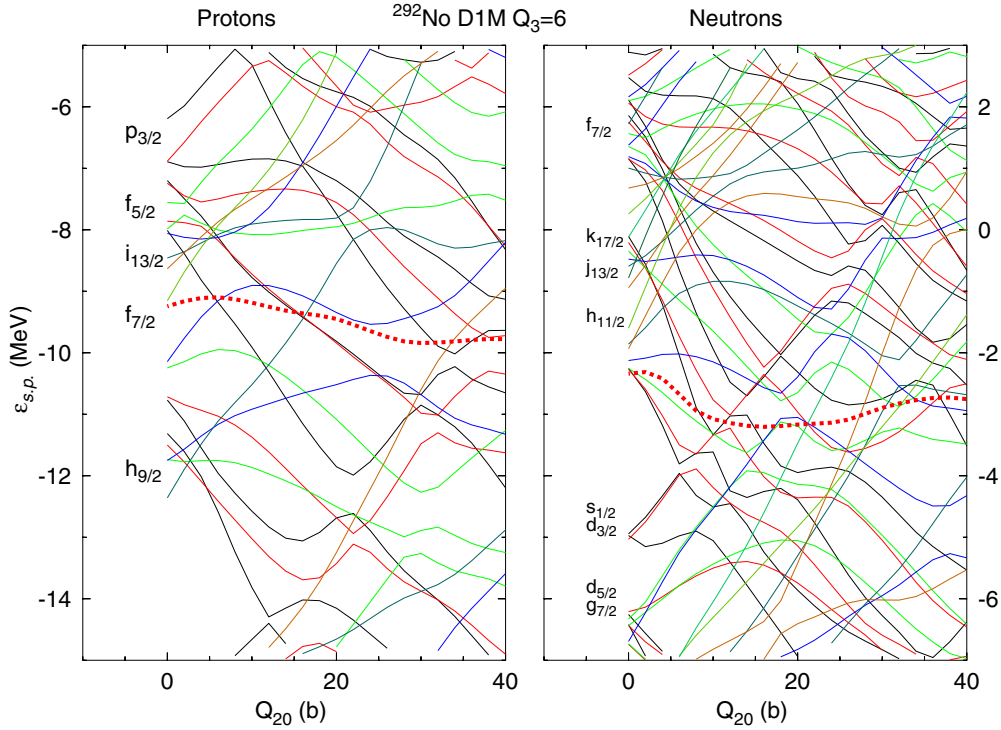

FIG. 4. Same as Fig. 3 but for reflection asymmetric shapes corresponding to $Q_{30} = 6\ \mathrm{b}^{3/2}$. In this case, the single-particle orbitals do not have a definite parity and therefore all of them are plotted with full lines.

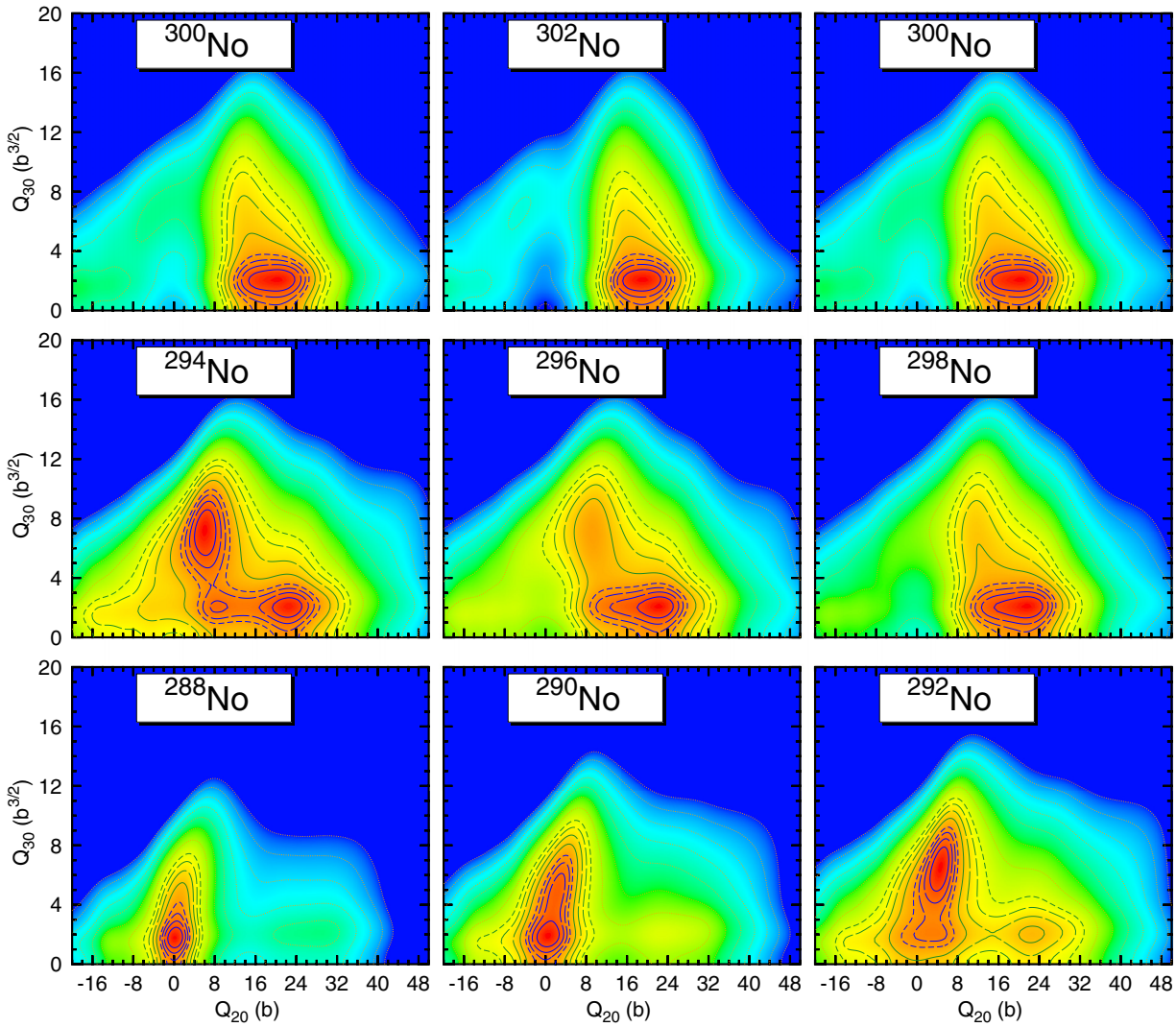

FIG. 5. Positive-parity ($\pi = +1$) PPPESs computed with the Gogny-D1M EDF for the isotopes $^{288-304}$No. See caption of Fig. 1 for the contour-line patterns and color scale.

$$- \lambda_Z \left(\frac{\langle \Phi(\mathbf{Q}) | \hat{Z} \hat{\mathcal{P}}^{\pi} | \Phi(\mathbf{Q}) \rangle}{\langle \Phi(\mathbf{Q}) | \hat{\mathcal{P}}^{\pi} | \Phi(\mathbf{Q}) \rangle} - Z_0 \right) - \lambda_N \left(\frac{\langle \Phi(\mathbf{Q}) | \hat{N} \hat{\mathcal{P}}^{\pi} | \Phi(\mathbf{Q}) \rangle}{\langle \Phi(\mathbf{Q}) | \hat{\mathcal{P}}^{\pi} | \Phi(\mathbf{Q}) \rangle} - N_0 \right). \quad (6)$$

Because the Gogny force used is a density-dependent one, we need a prescription for the density-dependent contribution to the energy overlaps. As in previous studies [53,54,59], we use the density

$$\rho(\vec{r}) = \frac{\langle \Phi(\mathbf{Q}) | \hat{\rho}(\vec{r}) | \Phi(\mathbf{Q}) \rangle}{\langle \Phi(\mathbf{Q}) | \Phi(\mathbf{Q}) \rangle} \quad (7)$$

to compute $\langle \Phi(\mathbf{Q}) | \hat{H}[\rho(\vec{r})] | \Phi(\mathbf{Q}) \rangle$ and the density

$$\theta(\vec{r}) = \frac{\langle \Phi(\mathbf{Q}) | \hat{\rho}(\vec{r}) \hat{\Pi} | \Phi(\mathbf{Q}) \rangle}{\langle \Phi(\mathbf{Q}) | \hat{\Pi} | \Phi(\mathbf{Q}) \rangle} \quad (8)$$

in the evaluation of $\langle \Phi(\mathbf{Q}) | \hat{H}[\theta(\vec{r})] \hat{\Pi} | \Phi(\mathbf{Q}) \rangle$. In this way, we avoid the pathologies found in the restoration of spatial symmetries [68–71]. As the parity-projected proton and neutron numbers usually differ from the nucleus's proton Z_0 and neutron N_0 numbers, we have introduced first-order corrections in Eq. (6), with λ_Z and λ_N being chemical potentials for protons and neutrons, respectively [53,54,59,72,73] .

The $\pi = +1$ and $\pi = -1$ PPPESs obtained for the isotopes $^{288-304}$No are depicted in Figs. 5 and 6 as illustrative examples. Since $\hat{\Pi} | \Phi(Q_{20}, Q_{30} = 0) \rangle = | \Phi(Q_{20}, Q_{30} = 0) \rangle$, the projection onto positive parity is unnecessary for those states. On the other hand, in the case of negative parity, the evaluation of the projected energy along the $Q_{30} = 0$ axis requires us to resolve 0/0 indeterminacy [36] and therefore it is subject to numerical inaccuracies [53,54]. However, the negative-parity projected energy $E_{\pi=-1}(\mathbf{Q})$ Eq. (6) increases rapidly when approaching $Q_{30} = 0$ (see Fig. 7) [53,54] and its limiting value [36] is high enough as not to play a significant role in the discussion of the $\pi = -1$ PPPESs. We have then omitted this quantity along the $Q_{30} = 0$ axis in Fig. 6. It is worthwhile to notice that the quadrupole moments corresponding to the absolute minima of the $\pi = +1$ and $\pi = -1$ PPPESs are close to the HFB values.

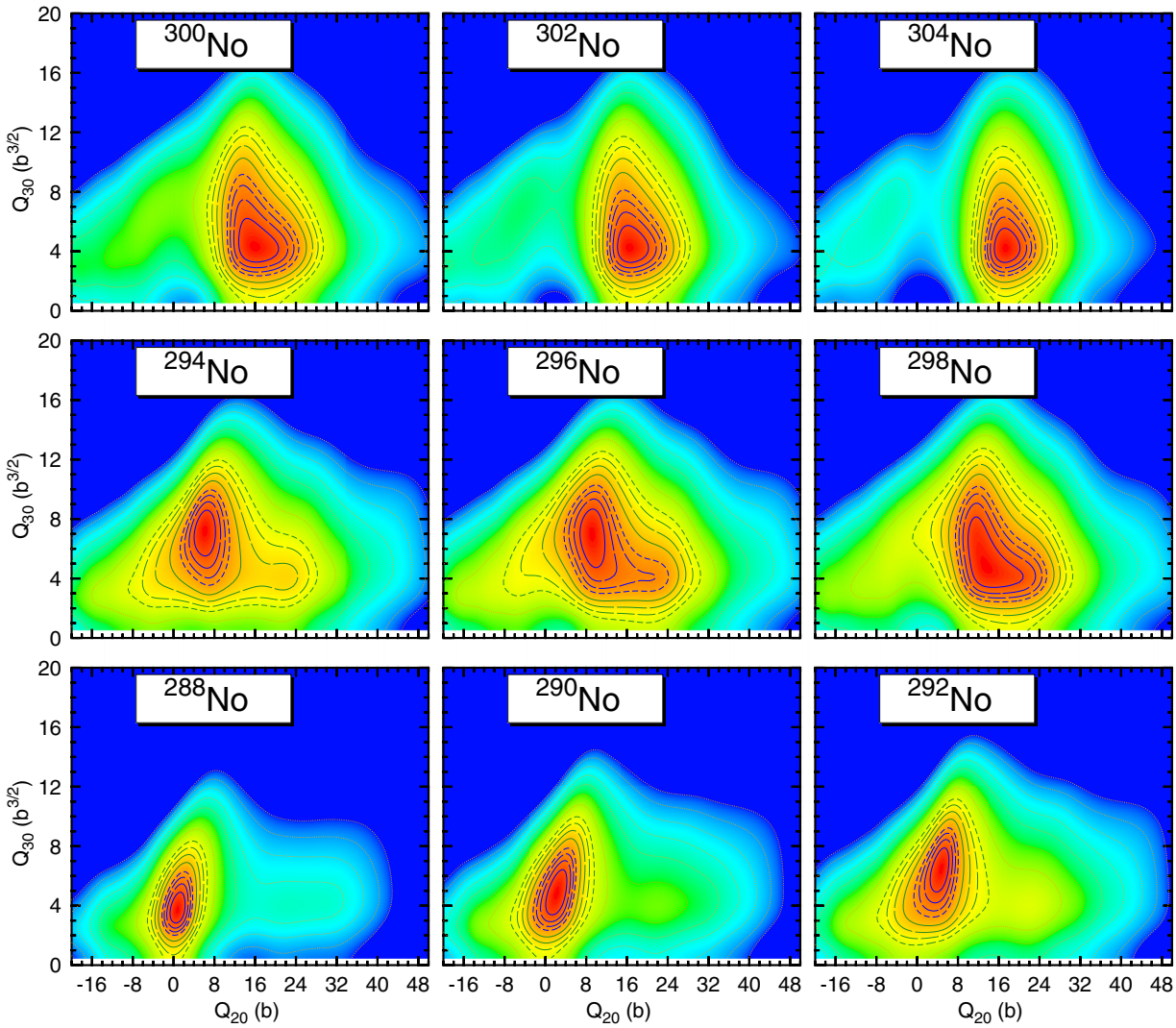

FIG. 6. Negative-parity ($\pi = -1$) PPPESs computed with the Gogny-D1M EDF for the isotopes $^{288-304}$No. See caption of Fig. 1 for the contour-line patterns and color scale.

As can be seen from Figs. 1, 5, and 7, not only the MF-PESs but also the $\pi = +1$ PPPESs are rather soft along the Q_{30} direction. In the case of nuclei with small and/or zero HFB ground-state octupole deformations, such as ^{288}No and ^{300}No, the $\pi = +1$ PPPESs only display an absolute minimum around $Q_{30} = 2.0$ b$^{3/2}$. This is illustrated in Figs. 7(a) and 7(c), where the $\pi = +1$ parity-projected energies obtained for ^{288}No and ^{300}No are plotted, as functions of Q_{30}, for a fixed value of the quadrupole moment corresponding to the absolute minimum of the PES. However, the topography along the Q_{30} direction is more complex for nuclei with larger HFB octupole deformations as the $\pi = +1$ PPPESs exhibit a pronounced competition between two minima. In the case of ^{294}No, for example, the energy difference between the local $Q_{30} = 2.0$b$^{3/2}$ and global $Q_{30} = 7.0$ b$^{3/2}$ minima [see Fig. 7(b)] amounts to 652 keV. Note also from Fig. 7(b), the energy degeneracy of the absolute HFB and $\pi = +1$ minima in this case. Furthermore, as can be seen from Fig. 5, for ^{294}No the shape coexistence extends to a third minimum, located at $(Q_{20}, Q_{30}) = (22$ b, 2 b$^{3/2})$, which is only 14 keV above the absolute one.

The $\pi = -1$ PPPESs, depicted in Fig. 6, exhibit in all the cases a well-developed absolute minimum. In the case of nuclei such as ^{288}No and ^{300}No, the absolute $\pi = -1$ minimum corresponds to a larger octupole deformation than the $\pi = +1$ one [see Figs. 7(a) and 7(c)]. On the other hand, for ^{294}No, the (degenerate) $\pi = -1$ and $\pi = +1$ absolute minima have similar octupole deformations [see Fig. 7(b)]. Similar features have been found for other isotopic chains. Let us mention that the complex topography found for the PPPESs along the Q_{30} direction in our Gogny-D1M calculations has already been studied, as a function of the strength of the two-body interaction, using parity projection on the Lipkin-Meshkov-Glick (LMG) model [74].

As a measure of the correlations induced by parity projection, we consider the correlation energy

$$\Delta E_{\mathrm{CORR},PP} = E_{\mathrm{HFB},GS} - E_{\pi=+1,GS}, \tag{9}$$

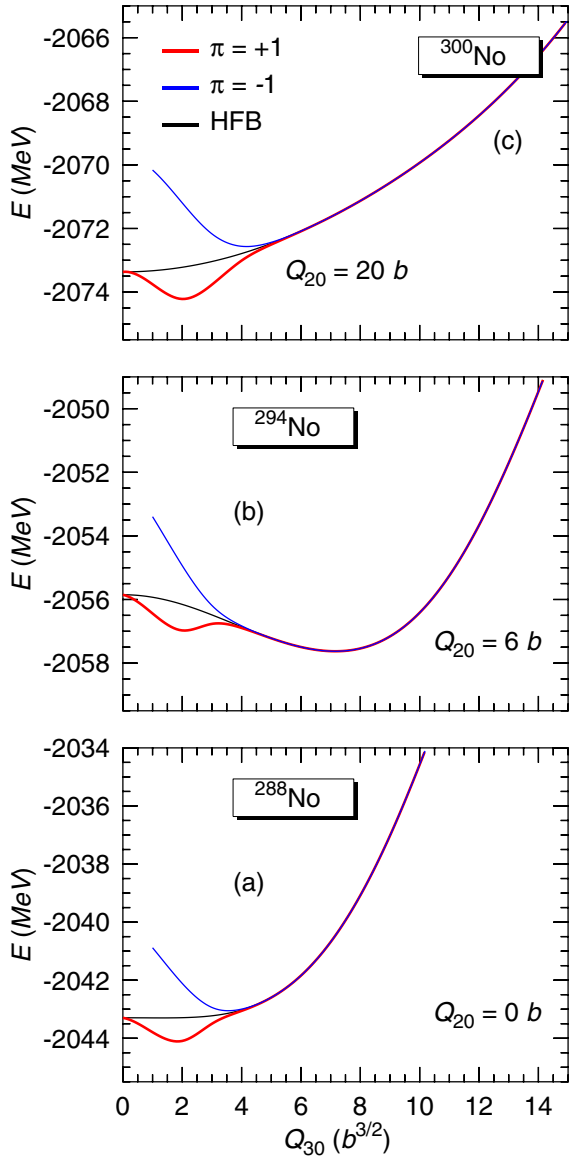

FIG. 7. The $\pi = +1$ (red) and $\pi = -1$ (blue) parity-projected energies are depicted as functions of the octupole moment Q_{30} for fixed values of the quadrupole moment Q_{20} in the nuclei ^{288}No, ^{294}No and ^{300}No. The corresponding HFB energies are also included in the plots. Results have been obtained with the Gogny-D1M EDF.

defined in terms of the difference between the HFB $E_{\mathrm{HFB},GS}$ and parity-projected $E_{\pi=+1,GS}$ ground-state energies. In Fig. 10, we show this quantity for the studied nuclei. The correlation energy $\Delta E_{\mathrm{CORR},PP}$ is zero or nearly zero for U, Pu, Cm, Cf, Fm, and No isotopes with $190 \leqslant N \leqslant 194$ as for these nuclei the $\pi = +1$ PPPESs display features, along the Q_{30} direction, similar to the ones discussed above for ^{294}No; i.e., the HFB and $\pi = +1$ absolute minima are degenerate or nearly degenerate. As will be discussed in Sec. II B 2, the comparison between the correlation energies $\Delta E_{\mathrm{CORR},PP}$ and the ones obtained within the symmetry-conserving 2D-GCM framework reveals the key role played by quantum fluctuations around those neutron numbers.

2. Generator coordinate method

The dynamical interplay between the quadrupole and octupole degrees of freedom is considered via the 2D-GCM ansatz

$$\left|\Psi^{\pi}_{\sigma}\right\rangle = \int d\mathbf{Q} f^{\pi}_{\sigma}(\mathbf{Q})|\Phi(\mathbf{Q})\rangle, \tag{10}$$

where both positive and negative octupole moments Q_{30} are included in the integration domain to assure the parity-conserving nature of the states $|\Psi^{\pi}_{\sigma}\rangle$ [53,54,59]. The index σ in Eq. (10) labels the different GCM solutions.

The amplitudes $f^{\pi}_{\sigma}(\mathbf{Q})$ are solutions of the Griffin-Hill-Wheeler (GHW) equation [58]

$$\int d\mathbf{Q}'(\mathcal{H}(\mathbf{Q},\mathbf{Q}') - E^{\pi}_{\sigma}\mathcal{N}(\mathbf{Q},\mathbf{Q}'))f^{\pi}_{\sigma}(\mathbf{Q}') = 0 \tag{11}$$

with the Hamiltonian and norm kernels given by

$$\begin{aligned}\mathcal{H}(\mathbf{Q},\mathbf{Q}') &= \langle\Phi(\mathbf{Q})|\hat{H}[\rho^{\mathrm{GCM}}(\vec{r})]|\Phi(\mathbf{Q}')\rangle \\ &\quad - \lambda_Z(\langle\Phi(\mathbf{Q})|\hat{Z}|\Phi(\mathbf{Q}')\rangle - Z_0\mathcal{N}(\mathbf{Q},\mathbf{Q}')) \\ &\quad - \lambda_N(\langle\Phi(\mathbf{Q})|\hat{N}|\Phi(\mathbf{Q}')\rangle - N_0\mathcal{N}(\mathbf{Q},\mathbf{Q}')), \\ \mathcal{N}(\mathbf{Q},\mathbf{Q}') &= \langle\Phi(\mathbf{Q})|\Phi(\mathbf{Q}')\rangle. \end{aligned} \tag{12}$$

As in previous studies [53,54,59], we use the *mixed* density prescription

$$\rho^{\mathrm{GCM}}(\vec{r}) = \frac{\langle\Phi(\mathbf{Q})|\hat{\rho}(\vec{r})|\Phi(\mathbf{Q}')\rangle}{\langle\Phi(\mathbf{Q})|\Phi(\mathbf{Q}')\rangle} \tag{13}$$

in the density-dependent term of the Hamiltonian kernel. As in the parity projection case Eq. (6), we use a perturbative first-order correction in the Hamiltonian kernel $\mathcal{H}(\mathbf{Q},\mathbf{Q}')$ to take into account deviations in both the proton and neutron numbers [53,59,72,73].

The HFB basis intrinsic states $|\Phi(\mathbf{Q})\rangle$ are not orthonormal. Therefore, the amplitudes $f^{\pi}_{\sigma}(\mathbf{Q})$ cannot be interpreted as probability amplitudes. Instead, one considers the so-called collective wave functions

$$G^{\pi}_{\sigma}(\mathbf{Q}) = \int d\mathbf{Q}'\mathcal{N}^{\frac{1}{2}}(\mathbf{Q},\mathbf{Q}')f^{\pi}_{\sigma}(\mathbf{Q}'), \tag{14}$$

written in terms of the operational square root of the norm kernel $\mathcal{N}^{\frac{1}{2}}(\mathbf{Q},\mathbf{Q}')$ [53,54,58,59,68].

The overlaps of one- and two-body operators between different HFB states are evaluated with the efficient Pfaffian techniques of Refs. [75–77].

For the reduced transition probabilities $B(E1, 1^- \to 0^+)$ and $B(E3, 3^- \to 0^+)$, the rotational formula for $K = 0$ bands has been used:

$$B(E\lambda, \lambda^- \to 0^+) = \frac{e^2}{4\pi}\left|\left\langle\Psi^{\pi=-1}_{\sigma}\middle|\hat{\mathcal{O}}_{\lambda}\middle|\Psi^{\pi'=+1}_{\sigma'=1}\right\rangle\right|^2. \tag{15}$$

For $B(E1)$ and $B(E3)$ transitions, σ corresponds to the first excited GCM state with negative parity. The electromagnetic transition operators $\hat{\mathcal{O}}_1$ and $\hat{\mathcal{O}}_3$ are the dipole moment operator and the proton component of the octupole operator, respectively [53]. The overlap $\langle\Psi^{\pi}_{\sigma}|\hat{O}|\Psi^{\pi'}_{\sigma'}\rangle$ of an operator $\hat{O}$ between

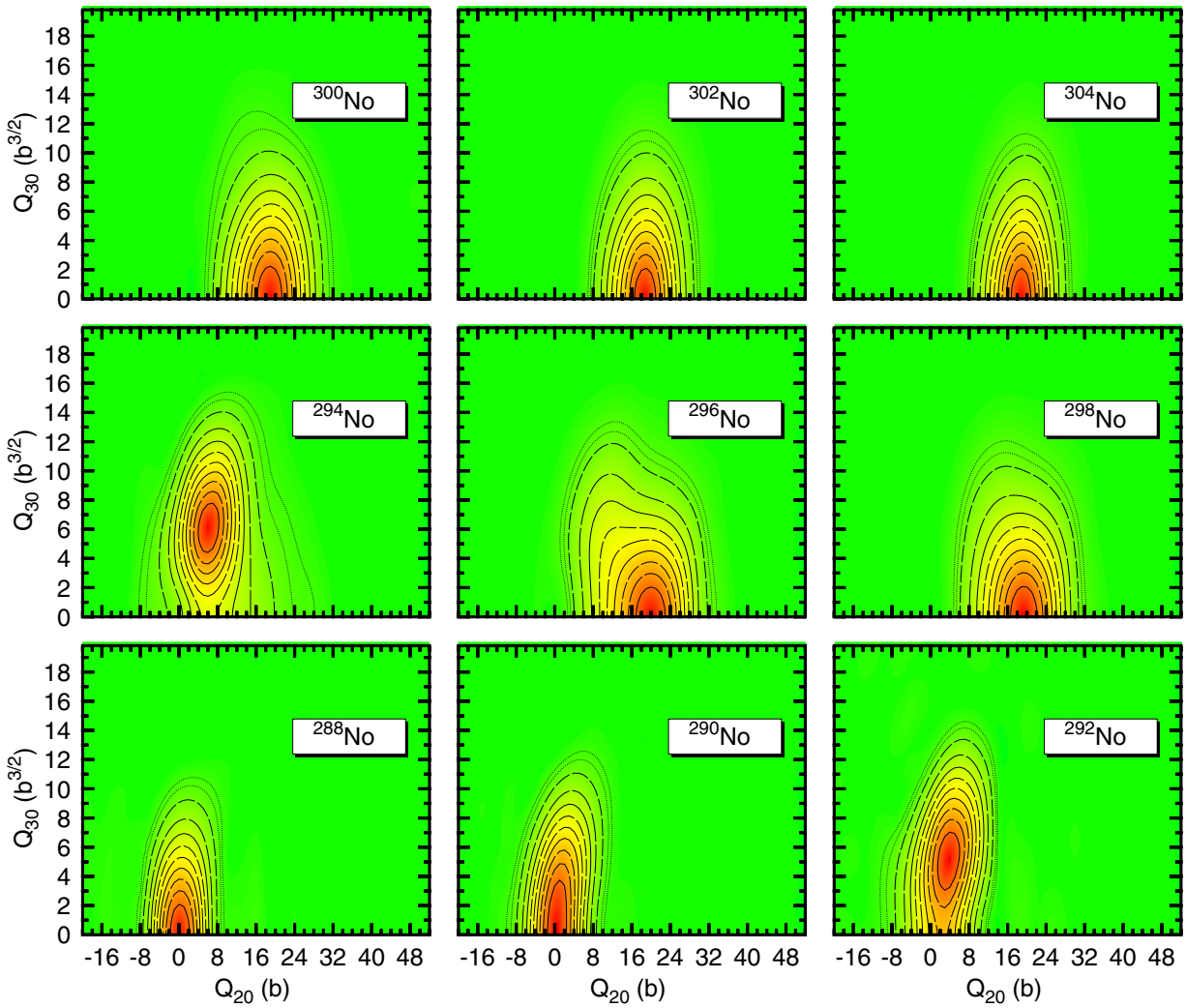

FIG. 8. Collective wave functions Eq. (14) for the ground states of the nuclei $^{288–304}$No. The contour lines (a succession of solid, long dashed, and short dashed lines) start at 90% of the maximum value up 10% of it. The two dotted-line contours correspond to the tail of the amplitude (5% and 1% of the maximum value). The color scale ranges from red (maximum value) to green (zero). Results have been obtained with the Gogny-D1M EDF. For more details, see the main text.

two different GCM states Eq. (10) can be evaluated according to the expressions given in Refs. [53,54].

The collective wave functions Eq. (14) corresponding to the ground and lowest negative-parity 2D-GCM states in $^{288–304}$No are plotted in Figs. 8 and 9, respectively. As can be seen from Fig. 8, the ground-state collective amplitude $G^{\pi=+1}_{\sigma=1}(Q_{20}, Q_{30})$ shows the typical Gaussian shape along both the quadrupole and octupole directions with a maximum located at octupole moments different from zero in ^{292,294}No. The same holds for ^{284,286}U, $^{286–290}$Pu, $^{286–290}$Cm, $^{288–292}$Cf, ^{290,292}Fm, ^{294}Rf, and ^{296}Sg. For other nuclei, the peaks of the ground-state collective amplitudes are located around $Q_{30} = 0$. The spreading of $G^{\pi=+1}_{\sigma=1}(Q_{20}, Q_{30})$ along the Q_{30} direction is large, indicating the octupole-soft character of the 2D-GCM ground states obtained for the considered nuclei. On the other hand, for the negative-parity amplitudes $G^{\pi=-1}_{\sigma}(Q_{20}, Q_{30})$, depicted in Fig. 9, the shape of the wave function is again Gaussian along the Q_{20} direction, whereas along the Q_{30} direction it shows the characteristic shape of the first excited state of the harmonic oscillator (odd under the exchange of sign in Q_{30}) with a zero value at $Q_{30} = 0$ as well as a maximum and a minimum, one at a positive Q_{30} value and the other at the corresponding negative value. As a consequence, the negative-parity wave function maximum or minimum always take place at a nonzero octupole moment. This is in agreement with the position of the minima of the $\pi = -1$ PPPESs (see Fig. 6).

The 2D-GCM average quadrupole moment is defined as

$$(\bar{Q}_{20})^{\pi}_{\sigma} = \left\langle \Psi^{\pi}_{\sigma} \middle| \hat{Q}_{20} \middle| \Psi^{\pi}_{\sigma} \right\rangle \tag{16}$$

and the ground-state values $(\bar{Q}_{20})^{\pi=+1}_{\sigma=1}$ corroborate the mean-field result; i.e., with increasing neutron number, for each of the studied isotopic chains, there is a transition to well quadrupole-deformed ground states. Similarly, the average quadrupole moments of the first negative-parity excited state $(\bar{Q}_{20})^{\pi=-1}_{\sigma}$ increase with increasing neutron number.

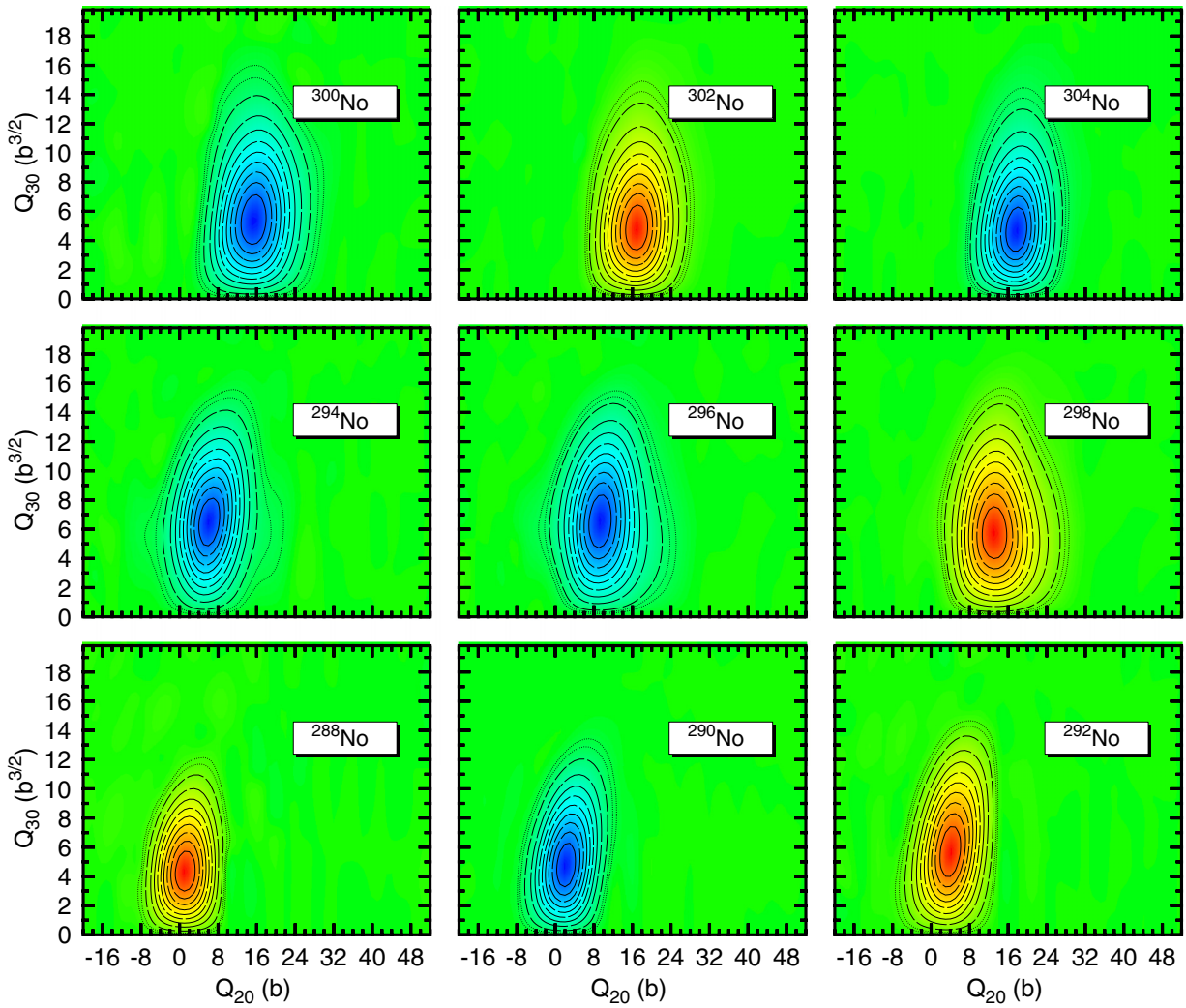

FIG. 9. Collective wave functions Eq. (14) for the lowest negative-parity states of the nuclei $^{288-304}$No. See the caption of Fig. 8 for contour-line patterns. Results have been obtained with the Gogny-D1M EDF. For more details, see the main text.

We have also computed the average octupole moment [53,54]

$$(\bar{Q}_{30})^{\pi}_{\sigma} = 4 \int_{\mathcal{D}} d\mathbf{Q} d\mathbf{Q}' G^{\pi *}_{\sigma}(\mathbf{Q}) \mathcal{Q}_{30}(\mathbf{Q}, \mathbf{Q}') G^{\pi}_{\sigma}(\mathbf{Q}') \quad (17)$$

and obtained, for all the studied nuclei, nonzero values in the range $0.37\ \mathrm{b}^{3/2} \leqslant (\bar{Q}_{30})^{\pi=+1}_{\sigma=1} \leqslant 5.41\ \mathrm{b}^{3/2}$. At variance with the static HFB results of Sec. II A, once parity-projected quadrupole-octupole configuration mixing effects are taken into account via the 2D-GCM ansatz Eq. (10), the ground states of all the studied nuclei are (dynamically) octupole-deformed, albeit with the largest octupole deformations $(\bar{Q}_{30})^{\pi=+1}_{\sigma=1}$ corresponding to U, Pu, Cm, Cf, Fm, No, Rf, and Sg isotopes with $190 \leqslant N \leqslant 196$. For the octupole moments $(\bar{Q}_{30})^{\pi=-1}_{\sigma}$, we have obtained values in the range $2.57\ \mathrm{b}^{3/2} \leqslant (\bar{Q}_{30})^{\pi=-1}_{\sigma} \leqslant 6.17\ \mathrm{b}^{3/2}$ and their largest values correspond once more to U, Pu, Cm, Cf, Fm, No, Rf, and Sg isotopes with $190 \leqslant N \leqslant 196$.

The 2D-GCM correlation energy

$$\Delta E_{\mathrm{CORR,2D-GCM}} = E_{\mathrm{HFB},GS} - E_{\pi=+1,\mathrm{2D-GCM}} \quad (18)$$

is defined as the difference between the HFB and 2D-GCM ground-state energies. This quantity is plotted in Fig. 10 along with the correlation energy $\Delta E_{\mathrm{CORR},PP}$ stemming from symmetry restoration alone. The comparison between both correlation energies reveals that 2D-GCM zero-point quantum fluctuations substantially modify the behavior of $\Delta E_{\mathrm{CORR},PP}$ for U, Pu, Cm, Cf, Fm, and No isotopes with $190 \leqslant N \leqslant 196$ providing a weaker dependence of $\Delta E_{\mathrm{CORR,2D-GCM}}$ with the neutron number. A weaker trend is also obtained for Rf and Sg nuclei around $N = 190$. This agrees well with previous results for Sm, Gd, and actinide nuclei [53,54]. Moreover, the range of values of the correlation energy $1.49\ \mathrm{MeV} \leqslant \Delta E_{\mathrm{CORR,2D-GCM}} \leqslant 2.45\ \mathrm{MeV}$ is of the same order of magnitude as the rms for the binding energy in Gogny-like nuclear mass tables [56] and, therefore, those correlation energies should be considered in future parametrizations of the Gogny-EDF.

The 2D-GCM energy difference between the positive-parity ground state and the lowest 1^- excited state is depicted in the left panels of Figs. 11 and 12 as a func-

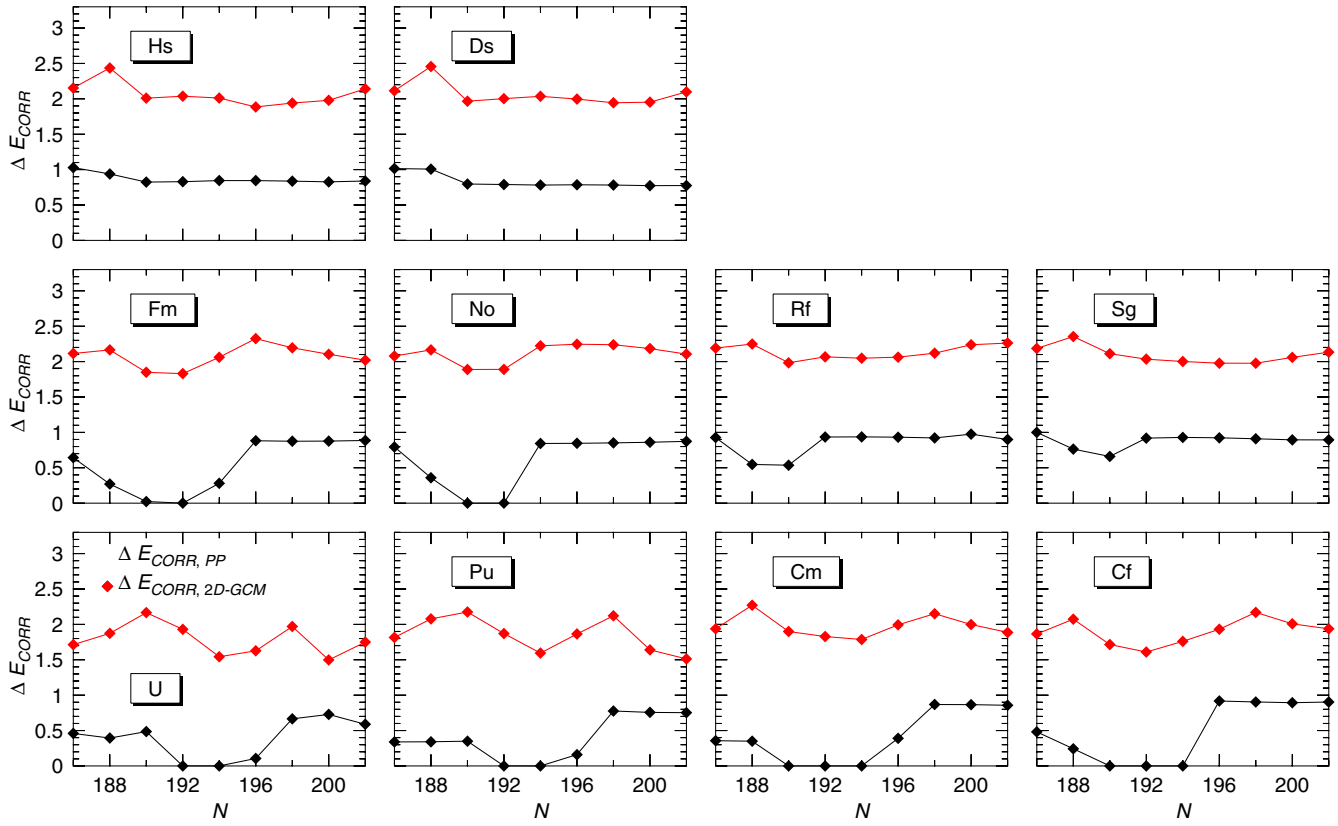

FIG. 10. The correlation energies obtained within the 2D-GCM framework Eq. (18) are plotted as functions of the neutron number. The correlation energies $\Delta E_{\mathrm{CORR},PP}$ Eq. (9) stemming from the restoration of reflection symmetry are also included in the plots. Results have been obtained with the Gogny-D1M EDF. For more details, see the main text.

tion of the neutron number. The 1^- excitation energies are very small ($0.10\,\mathrm{MeV} \leqslant E_{1^-} \leqslant 0.36\,\mathrm{MeV}$) for U, Pu, Cm, Cf, Fm, No, Rf, and Sg isotopes with $190 \leqslant N \leqslant 196$, in agreement with their large dynamical octupole deformations. Note that in the case of Hs and Ds isotopes, the E_{1^-} values obtained for ^{298}Hs (0.60 MeV) and ^{298}Ds (0.93 MeV) are slightly larger than the previous ones. Other nuclei, with less pronounced dynamical octupole deformation effects, exhibit larger E_{1^-} values, pointing toward the octupole vibrational character of their first negative-parity excited state. In the same panels, we have also included the E_{1^-} energies obtained within 1D-GCM calculations with Q_{30} as single generating coordinate. It is satisfying to observe that both calculations predict very similar trends with neutron number though the 2D-GCM energies are larger the the 1D-GCM ones.

The $B(E1)$ transition probabilities are plotted in the middle panels of Figs. 11 and 12. For $92 \leqslant Z \leqslant 102$, they exhibit a steady increase up to $N = 192$, while for larger neutron numbers, the $B(E1)$ strengths remain almost constant. Except for ^{298,300}Ds, a steady increase is also observed for $Z \geqslant 104$ up to $N = 190$. At variance with the results obtained for lower Z chains, except for ^{296}Rf and ^{298,300}Sg, the $B(E1)$ values also increase for larger neutron numbers, and the effect is more pronounced in the Hs and Ds isotopic chains. Note that the behavior of the $B(E1)$ strengths with neutron number is not correlated with the behavior of the negative-parity excitation energies and the $B(E3)$ strengths (discussed below). Therefore, it is not strictly correlated with the amount of octupole correlations. This is a consequence of the strong dependence of the dipole moment with orbital occupancies [35] that leads, for instance, to strong suppression of the $E1$ strength in some specific nuclei [39,78] and not in their neighbors. As can be seen from the figures, the $B(E1)$ transition probabilities obtained within 1D-GCM calculations exhibit the same pattern with neutron number as the 2D-GCM ones.

The $B(E3)$ transition probabilities are plotted in the right panels of Figs. 11 and 12. Unlike the $B(E1)$ case, the magnitude of the $B(E3)$ strength is strongly correlated with the excitation energy of the collective negative-parity state; i.e., whenever this excitation energy is small, the $B(E3)$ strength is large. Except for ^{296}No and ^{298}Rf, this correspondence is obeyed in all the considered nuclei. The MFPESs obtained for ^{296}No (see Fig. 1) and ^{298}Rf exhibit a pronounced competition between two minima at almost the same energy but with quite different Q_{20} and Q_{30} deformations. This shape coexistence leads to a rather low excitation energy of the 1^- state. However, the collective wave functions for the ground and negative-parity states barely overlap, leading to a reduction in the $B(E3)$ value. For other nuclei, the ground-state collective wave function is peaked at a nonzero octupole deformation and therefore strongly overlaps with the one of the negative-parity state (see Figs. 8 and 9), leading to a large $B(E3)$

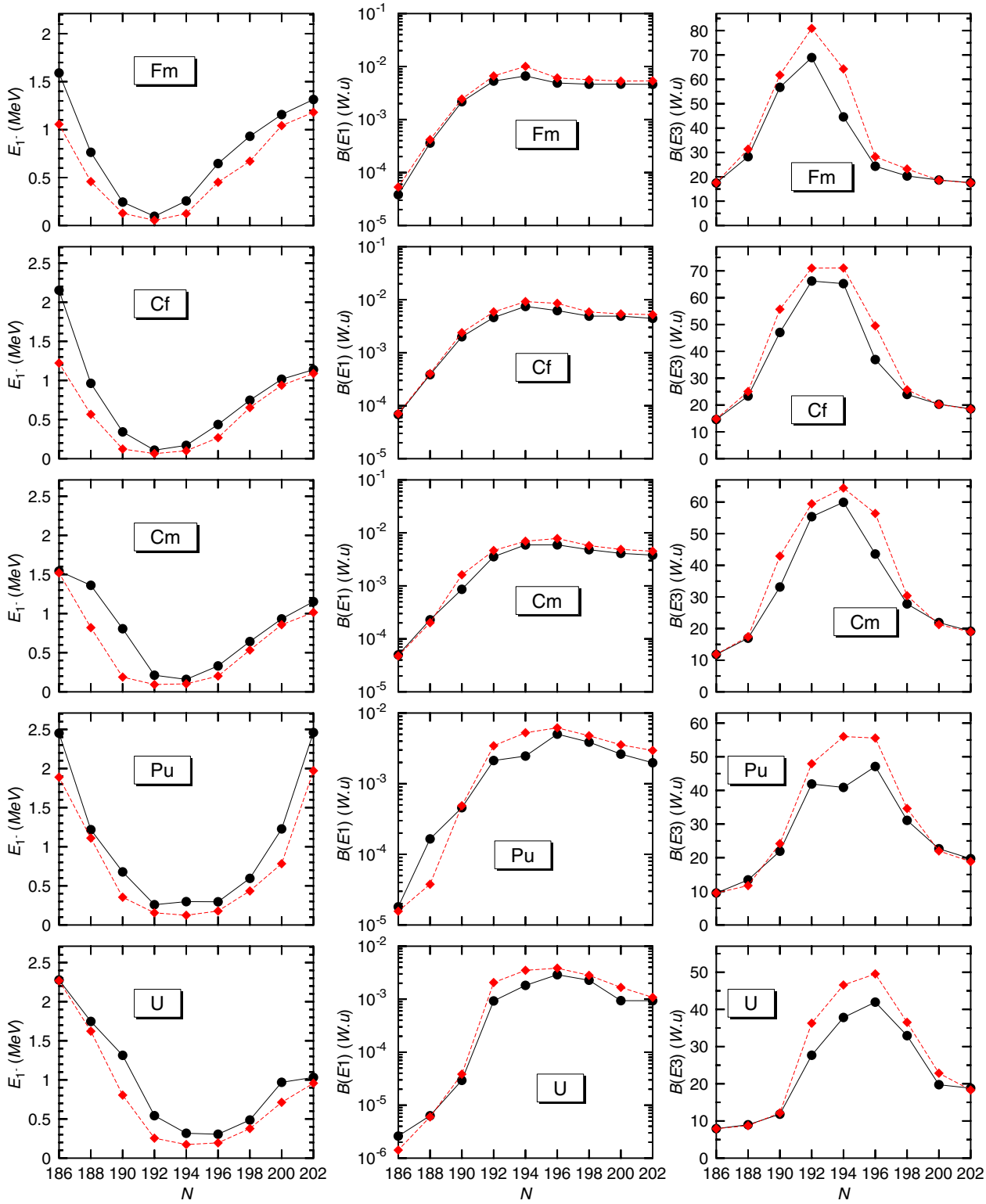

FIG. 11. The 2D-GCM E_{1^-} energy splittings (left panels) and the reduced transition probabilities $B(E1)$ (middle panels) and $B(E3)$ (right panels) are plotted (in black) as functions of the neutron number for the studied U, Pu, Cm, Cf, and Fm isotopic chains. The E_{1^-}, $B(E1)$, and $B(E3)$ values obtained in the framework of the 1D-GCM, with the octupole moment as single generating coordinate, have also been included (in red) in each of the plots. Results have been obtained with the Gogny-D1M EDF. For more details, see the main text.

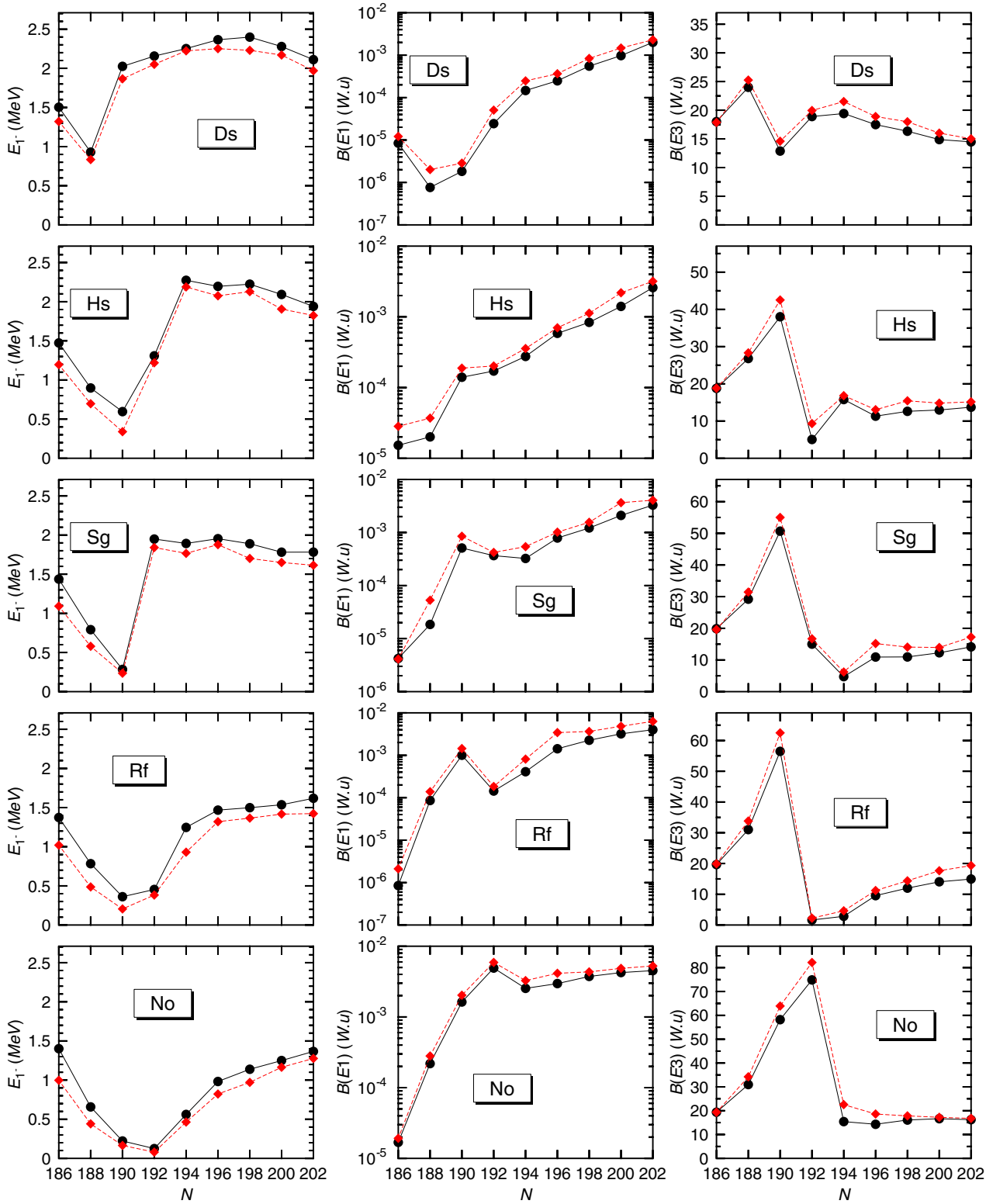

FIG. 12. The same as Fig. 11 but for the No, Rf, Sg, Hs, and Ds isotopic chains.

value. For less octupole correlated systems, the peak of the ground-state collective wave function shifts to $Q_{30} = 0$ and therefore the overlap with the negative-parity collective wave function is severely reduced as it is the $E3$ strength. As can be seen from the figures, the 1D-GCM and 2D-GCM $B(E3)$ transition probabilities display the same trend with the most pronounced quantitative differences being obtained for U, Pu, Cm, Cf, and Fm isotopes around $N = 194$.

In the comparison between 1D-GCM and 2D-GCM calculations, one should keep in mind that even when the

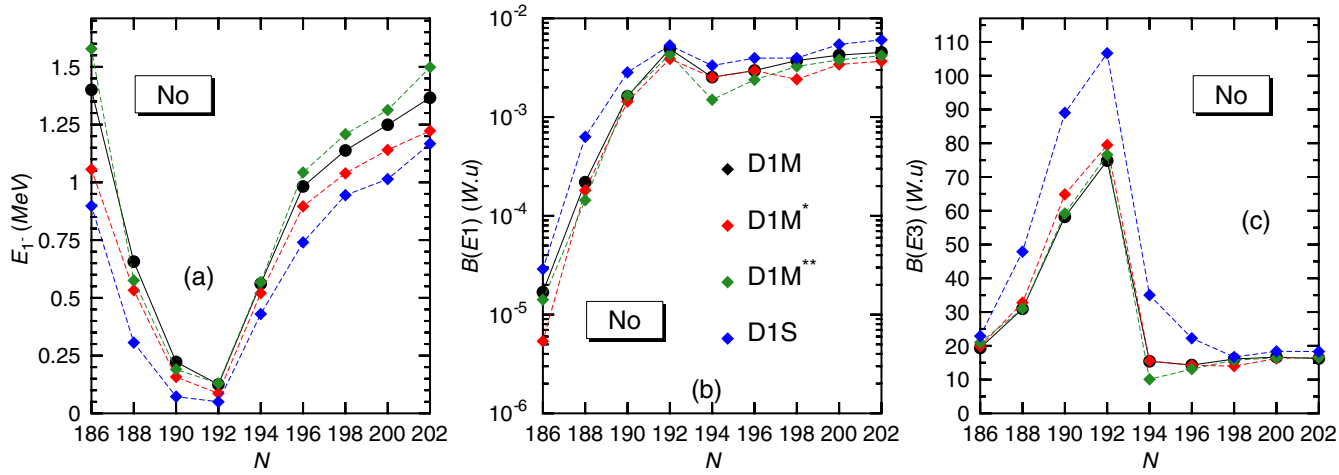

FIG. 13. The 2D-GCM E_{1^-} energy splittings [panel (a)] and the reduced transition probabilities $B(E1)$ [panel (b)] and $B(E3)$ [panel (c)] are plotted as functions of the neutron number for the isotopes $^{288-304}$No. Results have been obtained with the parametrizations D1S, D1M, D1M*, and D1M** of the Gogny-D1M EDF. For more details, see the main text.

corresponding collective wave functions look similar along the octupole direction, their tiny differences can be associated with the differences in the results. The comparison between 1D-GCM and 2D-GCM results in Figs. 11 and 12 reveals that, to a large extent, there is a decoupling between the quadrupole and octupole degrees of freedom in the studied nuclei, which indicates that the 1D-GCM framework represents a valuable computational tool to account for the systematics of the 1^- excitation energies and transition probabilities in this exotic region of the nuclear chart.

Finally, in order to illustrate the robustness of the 2D-GCM predictions with respect to the underlying Gogny-EDF, calculations have also been carried out with the parametrizations D1S, D1M*, and D1M** for $^{288-304}$No. The results are depicted in Fig. 13. The largest quantitative differences are obtained with the D1S parametrization, as expected, because D1M* and D1M** were fitted to be as close as possible to D1M. However, from the comparison we conclude that the predicted trends, with neutron number, of the 1^- excitation energies and reduced transition probabilities are rather insensitive to the Gogny-EDF employed in the calculations.

III. CONCLUSIONS

In this paper, we have studied the interplay between quadrupole and octupole degrees of freedom in a set of even-even neutron-rich actinides and superheavy nuclei with $92 \leqslant Z \leqslant 110$ and $186 \leqslant N \leqslant 202$, both at the mean-field level and beyond. To this end, we have resorted to the Gogny-HFB framework, parity projection, and 2D-GCM configuration mixing calculations with the quadrupole Q_{20} and octupole Q_{30} moments as generating coordinates.

Static octupole deformations are found around the "octupole neutron magic number," $N = 192$, in roughly 30% of the 90 nuclei analyzed. On the other hand, dynamical octupole deformations are ubiquitous and have a significant impact on correlation energies, leading to a weaker dependence with neutron number. The consideration of beyond-mean-field effects within the 2D-GCM approach allows us to explore properties of the lowest lying collective negative-parity excited states, such as their excitation energies and transition strengths to the positive-parity ground state. Low excitation energies and large $E3$ strengths are observed in nuclei with strong octupole correlations. The $E1$ strength, as expected, is a less collective quantity and does not show a clear correlation with octupole properties.

Given that very neutron-rich isotopes are considered, a comparison with experimental data is not possible at present and probably will not be possible in the future. However, the properties analyzed can be used to model the nuclear reactions taking place in the r-process nucleosynthesis of superheavy nuclei. The relevance of this lies on the fact that the population of short-lived superheavy nuclei is thought to have an impact on the solar abundance of midmass elements in the rare-earth-metal region through fission recycling.

ACKNOWLEDGMENTS

The work of L.M.R. was supported by Spanish Ministry of Economy and Competitiveness (MINECO) Grant No. PGC2018-094583-B-I00. We acknowledge the computer resources and assistance provided by Centro de Computacin Cientfica-Universidad Autnoma de Madrid (CCC-UAM).

[1] P. A. Butler and W. Nazarewicz, Rev. Mod. Phys. **68**, 349 (1996).

[2] R. Rodríguez-Guzmán and L. M. Robledo, Phys. Rev. C **89**, 054310 (2014).

[3] R. Rodríguez-Guzmán and L. M. Robledo, Eur. Phys. J. A **53**, 245 (2017).
[4] N. Schunck and L. M. Robledo, Rep. Prog. Phys. **79**, 116301 (2016).
[5] M. Warda and L. M. Robledo, Phys. Rev. C **84**, 044608 (2011).
[6] I. Ahmad and P. A. Butler, Ann. Rev. Nucl. Part. Sci. **43**, 71 (1993).
[7] P. A. Butler, J. Phys. G **43**, 073002 (2016).
[8] P. A. Butler and L. Willmann, Nucl. Phys. News **25**, 12 (2015).
[9] S. K. Tandel, M. Hemalatha, A. Y. Deo, S. B. Patel, R. Palit, T. Trivedi, J. Sethi, S. Saha, D. C. Biswas, and S. Mukhopadhyay, Phys. Rev. C **87**, 034319 (2013).
[10] H. J. Li, S. J. Zhu, J. H. Hamilton, E. H. Wang, A. V. Ramayya, Y. J. Chen, J. K. Hwang, J. Ranger, S. H. Liu, Z. G. Xiao, Y. Huang, Z. Zhang, Y. X. Luo, J. O. Rasmussen, I. Y. Lee, G. M. Ter-Akopian, Y. T. Oganessian, and W. C. Ma, Phys. Rev. C **90**, 047303 (2014).
[11] I. Ahmad, R. R. Chasman, J. P. Greene, F. G. Kondev, and S. Zhu, Phys. Rev. C **92**, 024313 (2015).
[12] B. Bucher, S. Zhu, C.Y. Wu, R.V.F. Janssens, D. Cline, A.B. Hayes, M. Albers, A.D. Ayangeakaa, P.A. Butler, C.M. Campbell *et al.*, Phys. Rev. Lett. **116**, 112503 (2016).
[13] B. Bucher, S. Zhu, C.Y. Wu, R.V.F. Janssens, R.N. Bernard, L.M. Robledo, T.R. Rodríguez, D. Cline, A.B. Hayes, A.D. Ayangeakaa *et al.*, Phys. Rev. Lett. **118**, 152504 (2017).
[14] P.A. Butler, L.P. Gaffney, P. Spagnoletti, K. Abrahams, M. Bowry, J. Cederkäll, G. de Angelis, H. De Witte, P.E. Garrett, A. Goldkuhle *et al.*, Phys. Rev. Lett. **124**, 042503 (2020).
[15] L. P. Gaffney, P. A. Butler, M. Scheck, A. B. Hayes, F. Wenander, M. Albers, B. Bastin, C. Bauer, A. Blazhev, S. Bönig *et al.*, Nature (London) **497**, 199 (2013).
[16] M. M. R. Chishti, D. O'Donnell, G. Battaglia, M. Bowry, D. A. Jaroszynski, B. S. Nara Singh, M. Scheck, P. Spagnoletti, and J. F. Smith, Nat. Phys. **16**, 853 (2020).
[17] L. I. Schiff, Phys. Rev. **132**, 2194 (1963).
[18] J. Dobaczewski, J. Engel, M. Kortelainen, and P. Becker, Phys. Rev. Lett. **121**, 232501 (2018).
[19] P. Möller and J. R. Nix, Nucl. Phys. A **361**, 117 (1981).
[20] A. Gyurkovich, A. Sobiczewski, B. Nerlo-Pomorska, and K. Pomorski, Phys. Lett. B **105**, 95 (1981).
[21] W. Nazarewicz, P. Olanders, I. Ragnarsson, J. Dudek, G. Leander, P. Möller, and E. Ruchowska, Nucl. Phys. A **429**, 269 (1984).
[22] P. Möller, J. Nix, W. D. Meyers, and W. Swiatecki, At. Data Nucl. Data Tables **59**, 185 (1995).
[23] P. Möller, R. Bengtson, B. G. Carlsson, P. Olivius, T. Ichikawa, H. Sagawa, and A. Iwamoto, At. Data Nucl. Data Tables **94**, 758 (2008).
[24] K. Nomura, D. Vretenar, T. Niksic, and B.-N. Lu, Phys. Rev. C **89**, 024312 (2014).
[25] K. Nomura, T. Niksic, and D. Vretenar, Phys. Rev. C **97**, 024317 (2018).
[26] K. Nomura, D. Vretenar, and B.-N. Lu, Phys. Rev. C **88**, 021303(R) (2013).
[27] K. Nomura, R. Rodríguez-Guzmán, and L. M. Robledo, Phys. Rev. C **92**, 014312 (2015).
[28] S. Marcos, H. Flocard, and P. H. Heenen, Nucl. Phys. A **410**, 125 (1983).
[29] P. Bonche, P.-H. Heenen, H. Flocard, and D. Vautherin, Phys. Lett. B **175**, 387 (1986).
[30] P. Bonche, S. J. Krieger, M. S. Weiss, J. Dobaczewski, H. Flocard, and P.-H. Heenen, Phys. Rev. Lett. **66**, 876 (1991).
[31] P.-H. Heenen, J. Skalski, P. Bonche, and H. Flocard, Phys. Rev. C **50**, 802 (1994).
[32] J. Erler, K. Langanke, H. P. Loens, G. Martínez-Pinedo, and P.-G. Reinhard, Phys. Rev. C **85**, 025802 (2012).
[33] L. M. Robledo, J. L. Egido, J. F. Berger, and M. Girod, Phys. Lett. B **187**, 223 (1987).
[34] L. M. Robledo, J. L. Egido, B. Nerlo-Pomorska, and K. Pomorski, Phys. Lett. B **201**, 409 (1988).
[35] J. L. Egido and L. M. Robledo, Nucl. Phys. A **518**, 475 (1990).
[36] J. L. Egido and L. M. Robledo, Nucl. Phys. A **524**, 65 (1991).
[37] E. Garrote, J. L. Egido, and L. M. Robledo, Phys. Rev. Lett. **80**, 4398 (1998); Nucl. Phys. A **654**, 723c (1999).
[38] L. M. Robledo, M. Baldo, P. Schuck, and X. Viñas, Phys. Rev. C **81**, 034315 (2010).
[39] J. L. Egido and L. M. Robledo, Nucl. Phys. A **545**, 589 (1992).
[40] W. H. Long, J. Meng, N. Van Giai, and S. G. Zhou, Phys. Rev. C **69**, 034319 (2004).
[41] R. N. Bernard, L. M. Robledo, and T. R. Rodríguez, Phys. Rev. C **93**, 061302(R) (2016).
[42] Z. Xu and Z.-P. Li, Chin. Phys. C **41**, 124107 (2017).
[43] Z. P. Li, B. Y. Song, J. M. Yao, D. Vretenar, and J. Meng, Phys. Lett. B **726**, 866 (2013).
[44] L. M. Robledo and R. Rodríguez-Guzmán, J. Phys. G: Nucl. Part. Phys. **39**, 105103 (2012).
[45] S. Ebata and T. Nakatsukasa, Phys. Scr. **92**, 064005 (2017).
[46] S. Y. Xia, H. Tao, Y. Lu, Z. P. Li, T. Niksic, and D. Vretenar, Phys. Rev. C **96**, 054303 (2017).
[47] S. E. Agbemava, A. V. Afanasjev, and P. Ring, Phys. Rev. C **93**, 044304 (2016).
[48] S. E. Agbemava and A. V. Afanasjev, Phys. Rev. C **96**, 024301 (2017).
[49] Y. Cao, S. E. Agbemava, A. V. Afanasjev, W. Nazarewicz, and E. Olsen, Phys. Rev. C **102**, 024311 (2020).
[50] L. M. Robledo and G. F. Bertsch, Phys. Rev. C **84**, 054302 (2011).
[51] L. M. Robledo, J. Phys. G: Nucl. Part. Phys. **42**, 055109 (2015).
[52] J. Dechargé and D. Gogny, Phys. Rev. C **21**, 1568 (1980).
[53] R. Rodríguez-Guzmán, L. M. Robledo, and P. Sarriguren, Phys. Rev. C **86**, 034336 (2012).
[54] R. Rodríguez-Guzmán, Y. M. Humadi, and L. M. Robledo, J. Phys. G: Nucl. Part. Phys. **48**, 015103 (2021).
[55] J. F. Berger, M. Girod, and D. Gogny, Nucl. Phys. A **428**, 23c (1984).
[56] S. Goriely, S. Hilaire, M. Girod, and S. Péru, Phys. Rev. Lett. **102**, 242501 (2009).
[57] C. Gonzalez-Boquera, M. Centelles, X. Vinas, and L. M. Robledo, Phys. Lett. B **779**, 195 (2018).
[58] P. Ring and P. Schuck, *The Nuclear Many-Body Problem* (Springer, Berlin, 1980).
[59] L. M. Robledo and P. A. Butler, Phys. Rev C **88**, 051302(R) (2013).
[60] P. Jachimowicz, M. Kowal, and J. Skalski, arXiv:2010.10018v1 [nucl-th].
[61] R. Rodríguez-Guzmán, Y. M. Humadi, and L. M. Robledo, Eur. Phys. J. A **56**, 43 (2020).
[62] M. Warda and J. L. Egido, Phys. Rev. C **86**, 014322 (2012).
[63] S. Goriely, A. Bauswein, and H.-T. Hanka, Astr. Phys. J. **738**, L32 (2011).

[64] O. Just, A. Bauswein, R. A. Pulpillo, S. Goriely, and H.-T. Hanka, Mont. Not. R. Astr. Soc. **448**, 541 (2015).
[65] L. M. Robledo, T. R. Rodríguez, and R. Rodríguez-Guzmán, J. Phys. G: Nucl. Part. Phys. **46**, 013001 (2019).
[66] X. Vinas, C. Gonzalez-Boquera, M. Centelles, C. Mondal, and L. M. Robledo, Acta Phys. Pol. B Proc. Suppl. **12**, 705 (2019).
[67] L. M. Robledo and G. F. Bertsch, Phys. Rev C **84**, 014312 (2011).
[68] R. R. Rodríguez-Guzmán, J. L. Egido, and L. M. Robledo, Nucl. Phys. A **709**, 201 (2002).
[69] J. L. Egido and L. M. Robledo, Lect. Notes Phys. **641**, 269 (2004).
[70] L. M. Robledo, Int. J. Mod. Phys. E **16**, 337 (2007).
[71] L. M. Robledo, J. Phys. G: Nucl. Part. Phys. **37**, 064020 (2010).
[72] K. Hara, A. Hayashi, and P. Ring, Nucl. Phys. A **385**, 14 (1982).
[73] P. Bonche, J. Dobaczewski, H. Flocard, P.-H. Heenen, and J. Meyer, Nucl. Phys. A **510**, 466 (1990).
[74] L. M. Robledo, Phys. Rev. C **46**, 238 (1992).
[75] L. M. Robledo, Phys. Rev. C **79**, 021302(R) (2009).
[76] L. M. Robledo, Phys. Rev. C **84**, 014307 (2011).
[77] G. F. Bertsch and L. M. Robledo, Phys. Rev. Lett. **108**, 042505 (2012)
[78] J. L Egido and L. M. Robledo, Nucl. Phys. A **494**, 85 (1989).